$S9-32$

$3 82272$

February 15, 1996

Modeling and Analysis of the DSS-14 Antenna Control System

W. Gawronski and R. Bartos
Communications Ground Systems Section

An improvement of pointing precision of the DSS-14 antenna is planned for the near future. In order to analyze the improvement limits and to design new controllers, a precise model of the antenna and the servo is developed, including a finite element model of the antenna structure and detailed models of the hydraulic drives and electronic parts. The DSS-14 antenna control system has two modes of operation: computer mode and precision mode. The principal goal of this investigation is to develop the model of the computer mode and to evaluate its performance. The DSS-14 antenna computer model consists of the antenna structure and drives in azimuth and elevation. For this model, the position servo loop is derived, and simulations of the closed-loop antenna dynamics are presented. The model is significantly different from that for the 34-m beam-waveguide antennas.

I. Introduction

The DSS-14 antenna control system model consists of the antenna structure, antenna drives in azimuth and elevation, and the position servo loop. Each drive, in turn, consists of gearboxes, hydraulic servo (active and passive valves, hydraulic lines, and hydraulic motors), and electronics boards (amplifiers and filters). The DSS-14 antenna control system model was developed by R. E. Hill [1,2]. In the present development, we obtain a more precise model that allows for accurate simulations of the antenna pointing errors and allows simulation of the intermediate variables, such as torques, currents, wheel rates, truss stresses, etc. We incorporate the finite element structural model with free rotation in azimuth and elevation, in a manner similar to the 34-m antenna models [3–5], that involves cross-coupling effects between azimuth and elevation, wind pressure on the dish, and pointing error model. The hydraulic part involves a recent development in modeling of the hydraulic components by R. Bartos [6–8].

The rate loop model consists of the elevation and azimuth drives and the antenna structure. Each drive consists of three major components: the electronics boards, hydraulic system, and gearbox. A model of each component is derived separately, then put together, forming the drive and rate loop models. Finally, the position loop is closed to obtain the position loop model.

II. Drive Model

A block diagram of the drive model is shown in Fig. 1, where N_t is the ratio between motor rate and tachometer (pinion) rate; r, rad/s, is the rate input to the drive; i, A, is the hydraulic active valve
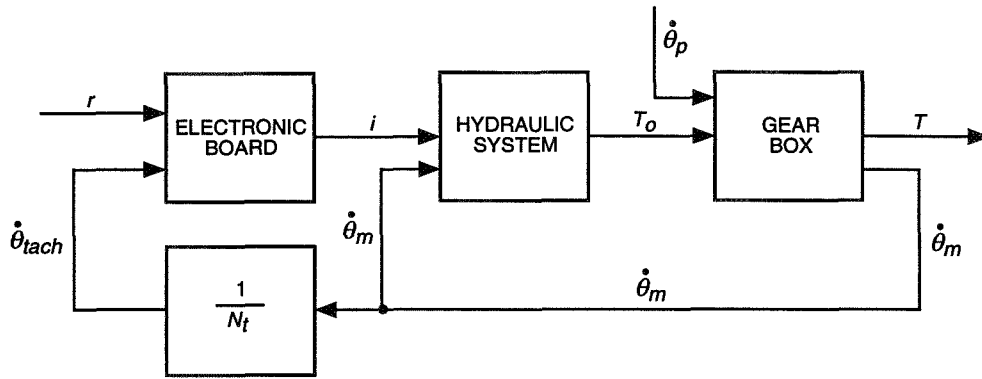
Fig. 1. Block diagram of the antenna drive.

solenoid current; T_o and T, N·m or lb in., are the gearbox and on-axis torques, respectively; and $\dot\theta_{tach}$ and $\dot\theta_m$, rad/s, are the pinion and motor rates, respectively. The state–space representation of the electronic board, hydraulic system, and gearbox are derived in the following sections.

A. Electronic Board

A schematic diagram for the electronic board is shown in Fig. 2. The inputs are the rate command r, rad/s, and the tachometer rate $\dot\theta_{tach}$, rad/s. The output is the solenoid valve current i. The scaling factors, k_r and k_t, convert the inputs into the command voltage, v_r, and tachometer voltage, v_t. The subsystem, G_t, is the tachometer circuit: it transforms the tachometer voltage, v_t, into the voltage, v_{to}. The subsystems with the transfer functions G_{r1} and G_{r2} are the rate amplifier circuits: they transform the command voltage, v_r, and the tachometer voltage, v_{to}, into the error voltage, v_s. The subsystem with the transfer function, G_s, is the valve driver amplifier circuit, with the error voltage, v_s, as the input and the valve current, i, as the output.
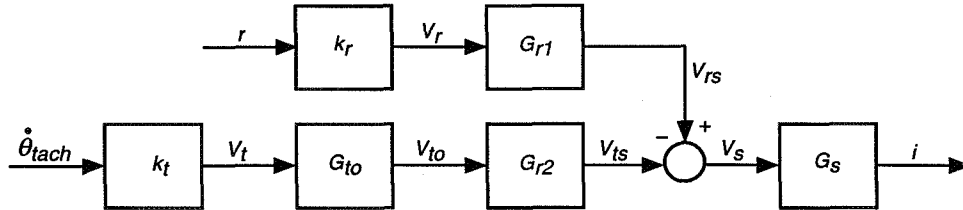

Fig. 2. Block diagram of the electronic board.

The following transfer functions of each of the four components are derived in the Appendix. The transfer function G_{to} for azimuth is

$$G_{to} = 0.151 \tag{1}$$

and, for elevation, is

$$G_{to} = 0.127 \tag{2}$$

The transfer functions G_{r1} (from v_r to v_s) and G_{r2} (from v_{to} to v_s) are

$$G_{r1} = 6.20 \ G_o \left.\begin{array}{c}\\\\\end{array}\right\} \tag{3}$$

$$G_{r2} = -4.65 \ G_o$$

where

$$G_o = \frac{1 + 0.400s}{1 + 4.205s} \tag{4}$$

is the transfer function of a lag compensator. The transfer function G_s is

$$G_s = 4.42 \times 10^{-5} \tag{5}$$

The scaling factors, k_r and k_t, are $k_r = 1212.6$ V/rad/s and $k_t = 2.5$ V/rad/s. Thus, the command transfer function from the rate command r to the solenoid current i_s is

$$G_r = k_r G_{r1} G_s = 0.3323 \ G_o \tag{6}$$

where G_o is defined in Eq. (4). The tachometer transfer function from the tachometer rate $\dot{\theta}_{tach}$ to the solenoid current i_s is

$$G_t = k_t G_{to} G_{r2} G_s \tag{7}$$

$$G_t = \begin{cases} -0.7750 \times 10^{-4} G_o & \text{for azimuth} \\ -0.6525 \times 10^{-4} G_o & \text{for elevation} \end{cases} \tag{8}$$

In order to check the correctness of the derivation, note that the ratio G_r/G_t should be equal to N_o, where N_o is the tachometer-to-axis ratio ($N_o = 4287.5$ for azimuth and $N_o = 5083.6$ for elevation). Indeed, from Eqs. (6) and (7), one obtains

$$\frac{G_r}{G_t} = \begin{cases} -4287.7 = N_o & \text{for azimuth} \\ -5092.7 \cong N_o & \text{for elevation} \end{cases} \tag{9}$$

Finally, the state–space representations of the transfer functions G_r and G_t (for azimuth and elevation) are easily obtained with the standard Matlab command in the form

$$\dot{x}_b = A_b x_b + B_{b1} r + B_{b2} \dot{\theta}_{tach} \left.\begin{array}{c}\\\\\end{array}\right\} \tag{10}$$

$$i = C_b x + D_{b1} r + D_{b2} \dot{\theta}_{tach}$$

The plot of the transfer function in azimuth (magnitude and phase) from r to i is shown in Fig. 3. The transfer function for elevation is identical. The plots of the transfer functions in azimuth and elevation from $\dot{\theta}_{tach}$ to i are shown in Fig. 4. The magnitudes drop in the frequency range from 0.01 to 0.1 Hz due to implementation of the filter G_o.
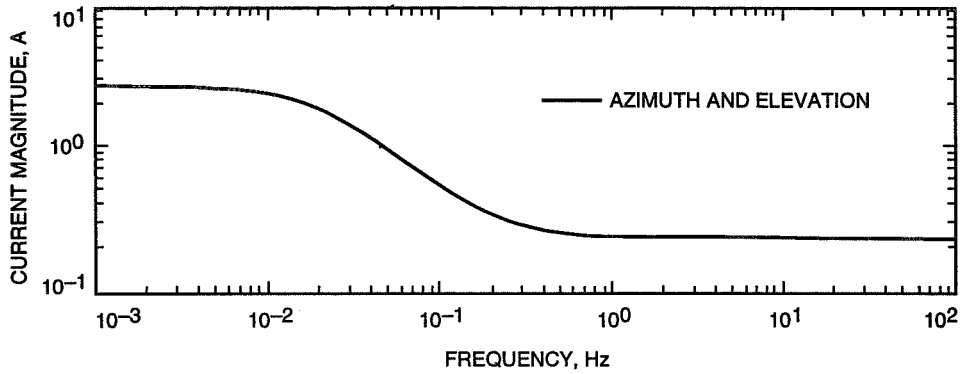
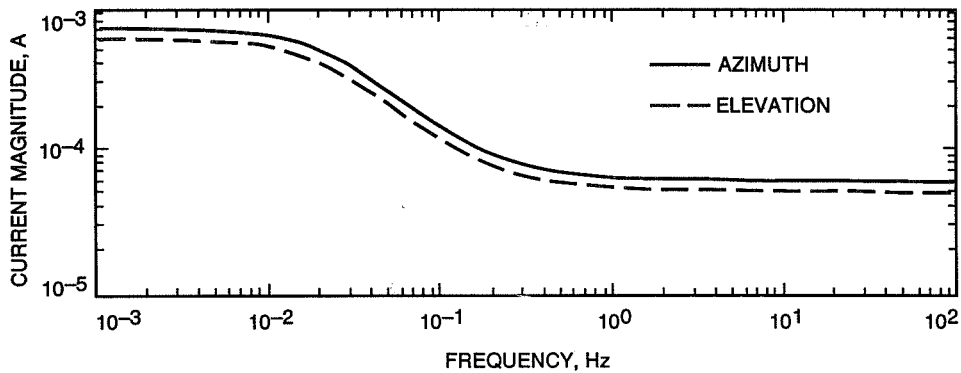**Fig. 3. Magnitude of the electronic board transfer function from the rate input to the board current.**

Fig. 4. Magnitude of the electronic board transfer function from the tachometer rate input to the board current.

B. Hydraulic System

The hydraulic servo system model was presented by R. E. Hill in [1] and [2]. Here we take a different approach, based on the recent investigations of hydraulic components by R. Bartos (see [6–8]). A block diagram of the DSS-14 hydraulic system is shown in Fig. 5. It consists of the hydraulic motor, shorting valve, hydraulic lines A and B, passive servo valves, and active servo valves. It has two inputs, servo valve current i and motor rate $\dot{\theta}_m$, and one output, motor torque T_o. The equations for each component are derived separately based on the work of Bartos [6–8]. Basically, these models are nonlinear ones; however, we linearize them in order to model the antenna linear regime of operation.

1. Active Servo Valve. This valve model has the input, i, A, and two outputs, q_{av}—the flow rate out of port a, cm^3/s, or in.^{3}/s, and q_{bv}, the flow rate out of port b, cm^3/s, or in.^{3}/s. From [6], one obtains

$$\ddot{q}_{av} + 2\zeta_o\omega_o\dot{q}_{av} + \omega_o^2 q_{av} = \omega_o^2 k_a i \tag{11a}$$

$$q_{bv} = -q_{av} \tag{11b}$$

where $\zeta_o = 0.8$ is the damping ratio, $\omega_o = 345.6$ rad/s is the valve natural frequency, and $k_a = 59,200$ − 97,300 cm^3/s/A (23,300–38300 in.^{3}/s/A) is the valve gain. The lower value is the Bartos estimate, while the upper value is the Hill estimate [2]. The values of the parameters are listed in Table 1.
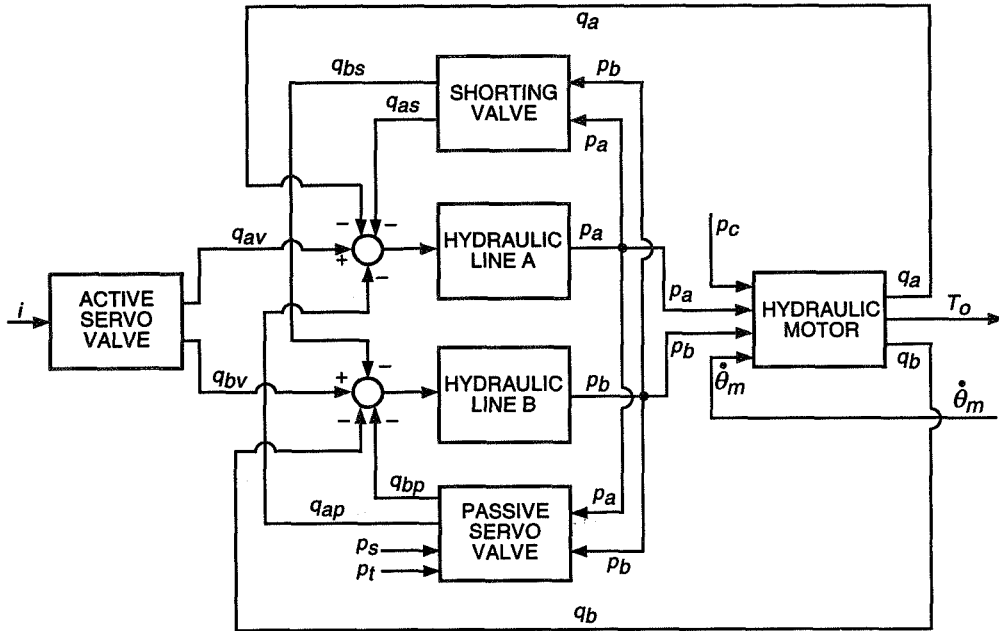
Fig. 5. Block diagram of the hydraulic drive.

Table 1. Parameters of the active servo valve (line A and line B).

Drive	ζ_o	ω_o, rad/s	k_a, cm^3/s/A	k_a, in.^{3}/s/A
Azimuth	0.6 to 0.8	345.56	59,200 to 97,300	23,300 to 38,300
Elevation	0.6 to 0.8	345.56	59,200 to 97,300	23,300 to 38,300

Introducing the new variable $q_v = q_{av} - q_{bv}$, one obtains from Eq. (11)

$$\ddot{q}_v + 2\zeta_o\omega_o\dot{q}_v + \omega_o^2 q_v = 2\omega_o^2 k_a i \qquad (12)$$

The differential variable q_v and the other differential variables introduced allow one to further simplify the analysis without loss of accuracy and to get rid of the "parasitic" variables, such as tank pressure, supply pressure, and case pressure.

2. Shorting Valve. The pressures p_a and p_b, kPa (lb/in.^{2}), are the inputs to the shorting valve, and the flows q_{as} and q_{bs}, cm^3/s (in.^{3}/s), are its output (see Fig. 5). The linearized relationship between the inputs and outputs is as follows:

$$\left. \begin{array}{l} q_{as} = k_s(p_a - p_b) \\ \\ q_{bs} = -q_{as} \end{array} \right\} \qquad (13)$$

where k_s is the valve gain, $k_s = 0.0007 - 0.007$ cm^3/s/kPa (0.0003–0.003 in.^{3}/s/psi), both in azimuth and elevation.

117

Introducing new differential variables $p = p_a - p_b$ and $q_s = q_{as} - q_{bs}$, one obtains Eq. (13) in the form

$$q_s = 2k_s p \tag{14}$$

3. Passive Servo Valve. This valve has four inputs: pressures p_a and p_b, supply pressure p_s, and tank pressure p_t. The last two are supplementary constant inputs that can be removed from the analysis. The valve has two outputs: flows q_{ap} and q_{bp}. Its linearized input–output relationship is as follows:

$$q_{ap} = k_{p1}(p_a - p_s) + k_{p2}(p_a - p_t) \tag{15a}$$

$$q_{bp} = k_{p1}(p_b - p_s) + k_{p2}(p_b - p_t) \tag{15b}$$

where the gains are $k_{p1} = 0.0055$ cm^3/kPa (0.00233 in.^{3}/psi) and $k_{p2} = k_{p1}$, the supply pressure is 17,240 kPa (2500 psi), and the tank pressure is 345 kPa (50 psi). These values are identical for azimuth and elevation.

Introducing $q_p = q_{ap} - q_{bp}$, and recalling that $p = p_a - p_b$, one obtains Eqs. (15a) and (15b) as follows:

$$q_p = (k_{p1} + k_{p2})p = 2k_p p \tag{16}$$

where, for simplicity of notation, we denote $k_p = k_{p1} = k_{p2}$.

4. Hydraulic Motor. The motor is described in [8]. From Fig. 5, it follows that the motor has four inputs and four outputs. The inputs are pressures p_a and p_b, case pressure p_c, and motor rate $\dot{\theta}_m$, rad/s. The outputs are flows q_a and q_b, leakage to the case q_c, and motor torque T_o, N·m (or lb in.). Following [8], one obtains the flow q_a from Eq. (59) of [8]:

$$q_a = q_{a1} + q_{a2} + q_{a3} \tag{17}$$

But, from Eq. (40) of [8],

$$q_{a1} = D\dot{\theta}_m \tag{18}$$

where $D = 6.3$ cm^3/rad (0.3836 in.^{3}/rad) is the motor "displacement." From Eq. (52) of [8], one obtains

$$q_{a2} = \frac{k_{a2}}{\mu}(p_a - p_c) \tag{19}$$

where $k_{a2} =$ from 6.35×10^{-5} to 18.3×10^{-5} cm^3 (from 2.5×10^{-5} to 7.2×10^{-5} in.^{3}) is the leakage constant (assumed to be 10^{-4} cm^3, or 4×10^{-5} in.^{3}); $\mu =$ from 2.8×10^{-4} to 2.8×10^{-3} kPa s (from 4×10^{-5} to 4×10^{-6} lb s/in.^{2}) is the absolute fluid viscosity (assumed to be 10^{-4} cm^3, or 4×10^{-5} in.^{3}); and $p_c = 221$ kPa (32 psi). From Eq. (58) of [8], one obtains the leakage from port A to port B, q_{a3}:

$$q_{a3} = \frac{k_{a3}}{\mu}(p_a - p_b) \tag{20}$$

where k_{a3} is the constant of proportionality determined through experiments. It is assumed to be equal to $k_{a2}, k_{a3} = k_{a2}$.

Combining Eqs. (17) through (20), one obtains

$$q_a = D\dot{\theta}_m + \frac{k_{a2} + k_{a3}}{\mu}p_a - \frac{k_{a3}}{\mu}p_b - \frac{k_{a2}}{\mu}p_c \qquad (21)$$

From [8], Eq. (60), one obtains the flow rate q_b:

$$q_b = q_{b1} + q_{b2} - q_{a3} \qquad (22)$$

It follows from [8], Eq. (41), that

$$q_{b1} = -q_{a1} = -D\dot{\theta}_m \qquad (23)$$

and from [8], Eq. (53), that

$$q_{b2} = \frac{k_{b2}}{\mu}(p_b - p_c) \qquad (24)$$

Combining Eqs. (22), (23), (24), and (20), one obtains

$$q_b = -D\dot{\theta} - \frac{k_{a3}}{\mu}p_a + \frac{k_{a3} + k_{b2}}{\mu}p_b - \frac{k_{b2}}{\mu}p_c \qquad (25)$$

The motor torque T_o is obtained from Eq. (28) of [8] by neglecting Coulomb friction and inertia torques (the latter are included in the gearbox model):

$$T_o = T_p + T_f \qquad (26)$$

where T_p is the torque generated by the motor and T_f is the viscous friction torque. The linearized Eq. (10) of [8] gives the torque generated by the motor:

$$T_p = D(p_a - p_b) \qquad (27)$$

and from Eq. (24) of [8], one obtains the viscous friction torque:

$$T_f = -k_v D\mu\dot{\theta} \qquad (28)$$

where $k_v = 0.0438$ is a dimensionless viscous friction coefficient. Combining Eqs. (26) through (28), one obtains

$$T_o = Dp_a - Dp_b - k_v D\mu\dot{\theta} \qquad (29)$$

Define $q = q_a - q_b$; then from Eqs. (21) and (25), one obtains

$$\left. \begin{array}{l} q = 2D\dot{\theta}_m + \dfrac{3k_{a2}}{\mu}p \\[2em] T_o = Dp - k_v D\mu\dot{\theta}_m \end{array} \right\} \tag{30}$$

The motor parameters are given in Table 2.

Table 2. Parameters of the hydraulic motor (line A and line B).

Drive	μ, kPa s	μ, lb s/in.^{2}	D, cm^3/rad	D, in.^{3}/rad	k_v	k_{a2}, cm^3	k_{a2}, in.^{3}	p_c, kPa	p_c, psi
Azimuth	2.8×10^{-4} to 28×10^{-4}	0.4×10^{-6} to 4×10^{-6}	25.2	1.52	0.0438	4.1×10^{-4} to 11.8×10^{-4}	2.5×10^{-5} to 7.2×10^{-5}	220	32
Elevation	2.8×10^{-4} to 28×10^{-4}	0.4×10^{-6} to 4×10^{-6}	25.2	1.52	0.0438	4.1×10^{-4} to 11.8×10^{-4}	2.5×10^{-5} to 7.2×10^{-5}	220	32

5. Hydraulic Line. There are two lines: A and B. A model for line A is developed, and the model for line B is similar (index "a" should be replaced with "b"). Line A has four inputs, flows q_a, q_{av}, q_{apv}, and q_{asv}, and a single output, pressure p_a (refer to Fig. 5). From [7], one obtains the line-A model as an integrator, with the negative feedback signs as in Fig. 5:

$$\dot{p}_a = k_{la}(-q_a + q_{av} - q_{ap} - q_{as}) \tag{31a}$$

Similarly, the line-B model is obtained:

$$\dot{p}_b = k_{lb}(-q_b + q_{bv} - q_{bp} - q_{bs}) \tag{31b}$$

As before, defining $p = p_a - p_b$, one obtains

$$\dot{p} = k_l(-q + q_v - q_p - q_s) \tag{32}$$

In these equations, the gains are

$$k_l = \frac{\beta}{v_o} \tag{33}$$

where β is the effective bulk modulus (capacitance of the line), $\beta = 1.29 \times 10^6$ kPa (1.87×10^5 psi), and v_o is the total volume, $v_o = 27{,}200$ cm^3 (1660 in.^{3}), so that $k_l = 47.3$ kPa/cm^3 (113 psi/in.^{3}). The values are collected in Table 3.

Table 3. Parameters of line A and line B.

Drive	β, kPa	β, psi	v_o, cm^3	v_o, in.^{3}
		Line A		
Azimuth	1.29×10^6	1.87×10^5	27,200	1653.6
Elevation	1.29×10^6	1.87×10^5	24,500	1498.1
		Line B		
Azimuth	1.29×10^6	1.87×10^5	27,700	1690.4
Elevation	1.29×10^6	1.87×10^5	24,600	1499.9

6. Hydraulic System Model. The model of the hydraulic system is derived by combining its elements (active servo valve, shorting valve, passive valve, hydraulic lines, and hydraulic motors). By introducing the new differential variables, the block diagram in Fig. 5 is simplified to the one in Fig. 6. A detailed block diagram of the hydraulic system is shown in Fig. 7. Combining Eqs. (12), (14), (16), (32), and (30) (or, alternatively, using the block diagram in Fig. 7), and defining the new state vector $x_h = [x_1, x_2, x_3]^T$, with three states, $x_1 = \dot{q}_v, x_2 = q_v$, and $x_3 = p$, and defining the input current, i, motor rate $\dot{\theta}_m$, and the single-output motor torque, T_o, one obtains

$$\left.\begin{array}{l} \dot{x}_h = A_h x_h + B_{ho}\dot{\theta}_m + B_{hi}i \\[2mm] T_o = C_h x_h + D_{ho}\dot{\theta}_m + D_{hi} \end{array}\right\} \qquad (34a)$$
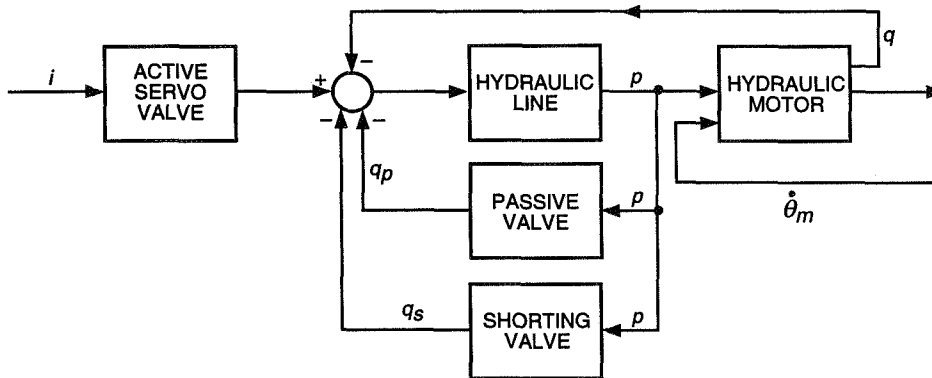
where

Fig. 6. Simplified block diagram of the hydraulic drive.

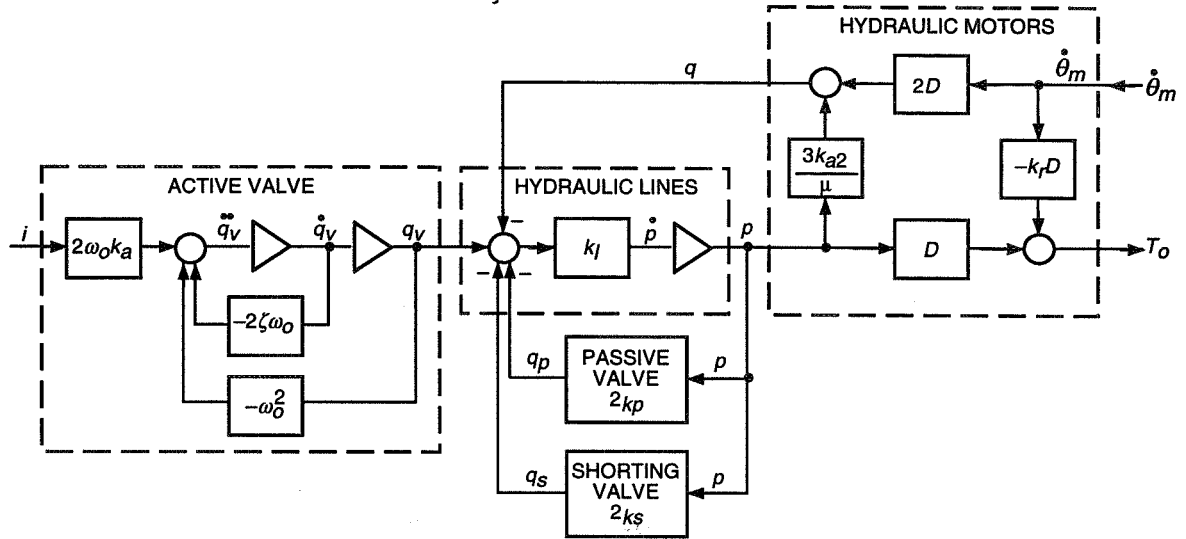**Fig. 7. Detailed block diagram of the hydraulic system.**

$$A_h = \begin{bmatrix} -2\zeta_o\omega_o & -\omega_o^2 & 0 \\ 1 & 0 & 0 \\ 0 & k_l & k_l\left(-\dfrac{3k_{a2}}{\mu} - 2k_p - 2k_s\right) \end{bmatrix}$$

$$B_{hi} = \begin{bmatrix} 2\omega_o^2 k_a \\ 0 \\ 0 \end{bmatrix}$$

$$B_{ho} = \begin{bmatrix} 0 \\ 0 \\ -2k_l D \end{bmatrix}$$

$$C_h = \begin{bmatrix} 0 \\ 0 \\ D \end{bmatrix}$$

$$D_{hi} = 0$$

$$D_{ho} = -k_v D\mu$$

(34b)

The plots of the magnitudes of the transfer function in azimuth and elevation from i to T_o are shown in Fig. 8. The plots of the magnitudes of the transfer functions in azimuth and elevation from $\dot{\theta}_m$ to T_o are shown in Fig. 9.

C. Gearbox Model

The gearbox model was described in detail in [5], and its block diagram is given in Fig. 10. In this diagram, T_o is the motor torque, $\dot{\theta}_p$ is the antenna angular rate, ω_m is the motor rate, T is the gearbox
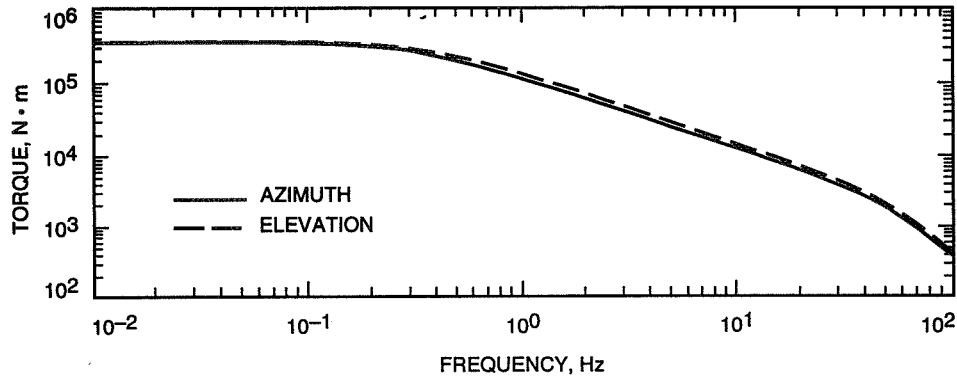
Fig. 8. Magnitude of the hydraulic drive transfer function from the solenoid current to the output torque.
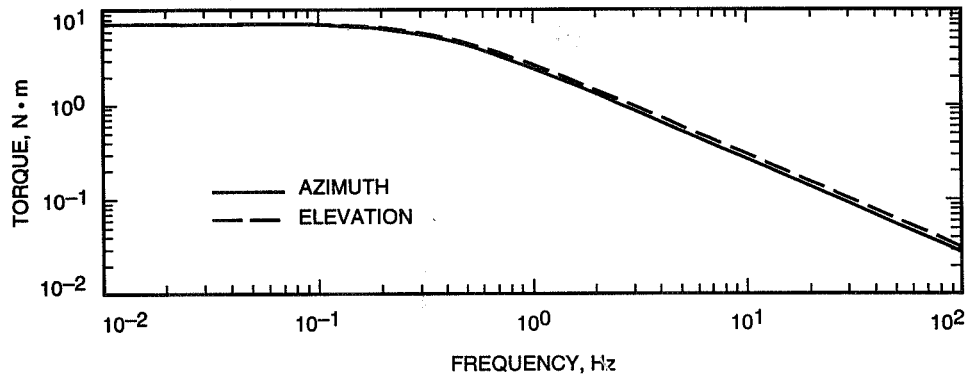

Fig. 9. Magnitude of the hydraulic drive transfer function from the motor rate to the output torque.
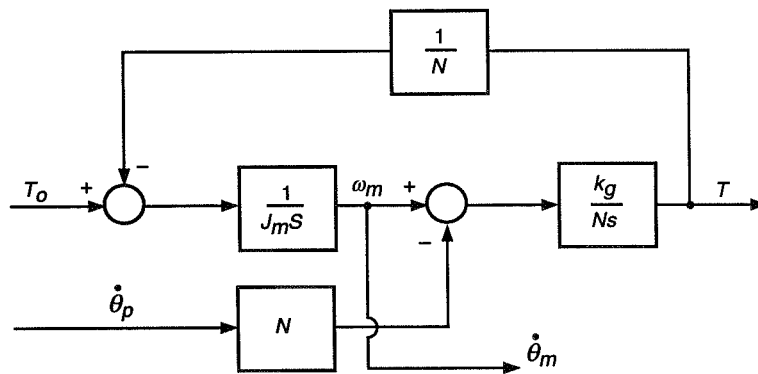

Fig. 10. Block diagram of the gearbox.

torque, J_m is the motor inertia, k_g is the gearbox (output) stiffness, and N is the gearbox ratio. This model has two inputs, the motor torque, T_o, and the wheel (pinion) angular rate, $\dot{\theta}_p$, and a single output, the gearbox torque, T.

The equations for this system are as follows:

$$J_m \dot{\omega}_m = T_o - \frac{T}{N} \tag{35a}$$

$$T = k_g \left(\frac{\theta_m}{N} - \theta_p \right) \tag{35b}$$

Denoting the state variables $x_1 = \omega_m$ and $x_2 = T$, one obtains

$$\dot{x}_1 = \frac{-x_2}{N J_m} + \frac{T_o}{J_m} \tag{36a}$$

$$\dot{x}_2 = \frac{k_g x_1}{N} - k_g \dot{\theta}_p \tag{36b}$$

Defining the gearbox state as $x_g = [\,x_1 \quad x_2\,]^T$, input T_o and $\dot{\theta}_p$, and output T and ω_m, one obtains the gearbox state–space representation (A_g, B_g, C_g):

$$\left. \begin{array}{l} \dot{x}_g = A_g x_g + B_{g1} T_o + B_{g2} \dot{\theta}_p \\[2mm] T = C_{g1} x_g \\[2mm] \dot{\theta}_m = C_{g2} x_g \end{array} \right\} \tag{37a}$$

where

$$\left. \begin{array}{l} A_g = \begin{bmatrix} 0 & \dfrac{-1}{N J_m} \\[3mm] \dfrac{k_g}{N} & 0 \end{bmatrix} \\[10mm] B_{g1} = \begin{bmatrix} \dfrac{1}{J_m} \\[3mm] 0 \end{bmatrix} \\[8mm] B_{g2} = \begin{bmatrix} 0 \\ -k_g \end{bmatrix} \\[6mm] C_{g1} = [\,0 \quad 1\,] \\[3mm] C_{g2} = [\,1 \quad 0\,] \end{array} \right\} \tag{37b}$$

D. Drive Model

The drive model is obtained by combining the state–space representation of the electronic board, Eq. (10); the hydraulic system, Eq. (34); and the gearbox, Eq. (37), according to the block diagram in Fig. 1. Defining the drive state vector $x_d = [x_b^T, x_h^T, x_g^T]^T$, we obtain the state equations

$$\dot{x}_d = A_d x_d + B_{dr} r + B_{dt} \dot{\theta}_p \left.\vphantom{\begin{matrix}1\\1\end{matrix}}\right\} \tag{38a}$$

$$T = C_d x_d$$

where

$$A_d = \begin{bmatrix} A_b & 0 & \dfrac{B_{b2} C_{g2}}{N_t} \\[2ex] B_{hi} C_b & A_h & B_{ho} C_{g2} + \dfrac{B_{hi} D_{be} C_{g2}}{N_t} \\[2ex] B_{g1} D_{hi} C_b & B_{g1} C_h & A_g + B_{g1} D_{ho} C_{g2} + \dfrac{B_{g1} D_{hi} D_{b2} C_{g2}}{N_t} \end{bmatrix}$$

$$B_{dr} = \begin{bmatrix} B_{b1} \\ B_{hi} D_{b1} \\ B_{g1} D_{hi} D_{b1} \end{bmatrix} \tag{38b}$$

$$B_{dt} = \begin{bmatrix} 0 \\ 0 \\ B_{g2} \end{bmatrix}$$

$$C_d = \begin{bmatrix} 0 & 0 & C_{g1} \end{bmatrix}$$

The plots of the magnitudes of the transfer function in azimuth and elevation from r to T are shown in Fig. 11. The plots of the transfer functions in azimuth and elevation from $\dot{\theta}_p$ to T are shown in Fig. 12.

III. Structure Model

The structural model is derived from the finite element model of the antenna structure with free rotations with respect to the elevation and azimuth axes. The finite element model consists of the diagonal modal mass $M_m(p \times p)$, diagonal natural frequencies matrix $\Omega(p \times p)$, diagonal modal damping matrix $Z(p \times p)$, and modal matrix $\Phi(m \times p), p \leq m$, which consists of p eigenvectors ϕ_i (mode shapes), $i = 1, \cdots, p$:

$$\Phi = [\phi_1, \phi_2, \cdots, \phi_p] \tag{39}$$

Let the finite element model have m degrees of freedom, with s inputs $u(t)$, where u is $s \times 1$ vector, and with r outputs $y(t)$, where y is $r \times 1$ vector. If the input matrix is $B_o(m \times s)$, the output matrix for displacement is $C_{oq}(r \times m)$, and the output matrix for rates is $C_{ov}(r \times m)$, then the input–output relationship is given by the following second-order differential equation:

$$\ddot{q}_m + 2Z\Omega\dot{q}_m + \Omega^2 q_m = M_m^{-1} \Phi^T B_o u \left.\vphantom{\begin{matrix}1\\1\end{matrix}}\right\} \tag{40}$$

$$y_m = C_{oq} \Phi q_m + C_{ov} \Phi \dot{q}_m$$
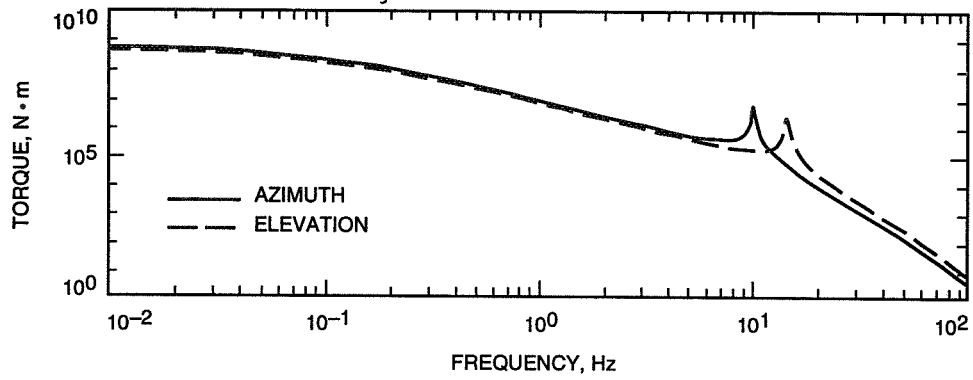
Define the state variable x as follows:

Fig. 11. Magnitude of the drive transfer function from the rate command to the output torque.
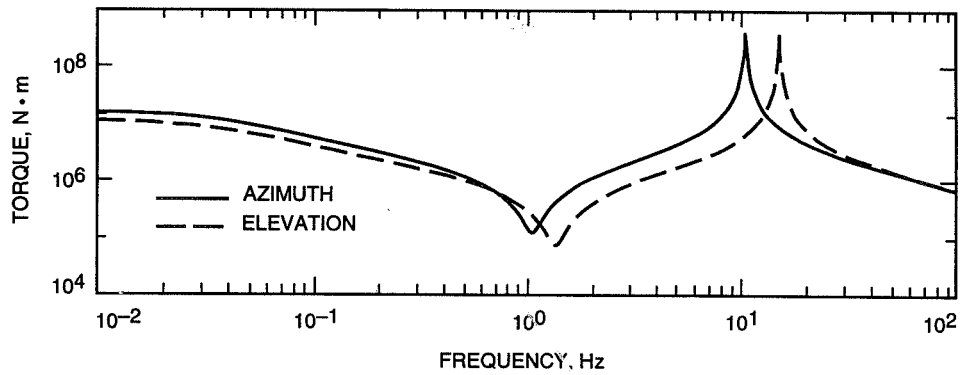

Fig. 12. Magnitude of the drive transfer function from the pinion rate to the output torque.

$$x_s = \begin{bmatrix} x_1 \\ x_2 \end{bmatrix} = \begin{bmatrix} q_m \\ \dot{q}_m \end{bmatrix} \tag{41}$$

where q_m and $\dot{q}_m$ are modal displacements and rates (such that $q = \Phi q_m$; q is the actual displacement); then Eq. (40) can be presented as a set of first-order equations:

$$\left. \begin{aligned} \dot{x}_1 &= x_2 \\ \dot{x}_2 &= -\Omega^2 x_1 - 2Z\Omega x_2 + M_m^{-1}\Phi B_o u_s \\ y_s &= C_{oq}\Phi x_1 + C_{ov}\phi x_2 \end{aligned} \right\} \tag{42}$$

or in the following form:

$$\left. \begin{aligned} \dot{x}_s &= A_s x_s + B_s u_s \\ y_s &= C_s x \end{aligned} \right\} \tag{43a}$$

126

where

$$A_s = \begin{bmatrix} 0 & I \\ -\Omega^2 & -2Z\Omega \end{bmatrix}$$

$$B_s = \begin{bmatrix} 0 \\ M_m^{-1}\Phi^T B_o \end{bmatrix} \qquad (43b)$$

$$C_s = [\, C_{oq}\Phi \quad C_{ov}\Phi \,]$$

is the sought state–space model in modal coordinates. In our case, $u_s = [\, T_a \quad T_e \,]$, where T_a and T_e are torques at azimuth wheels and elevation pinions, respectively. The structure output consists of the elevation and azimuth encoder angles and rates, pinion angles, elevation and cross-elevation pointing errors, and other structural variables of interest. Two outputs, $\dot{\theta}_{pa}$ and $\dot{\theta}_{pe}$, the pinion rates in azimuth and elevation, are of special interest. Thus, the structural state–space equations are as follows:

$$\dot{x}_s = A_s x_s + B_{sa} T_a + B_{se} T_e$$

$$\dot{\theta}_{pa} = C_{pa} x_s$$

$$\dot{\theta}_{pe} = C_{pe} x_s \qquad (44)$$

$$y = C_s x$$

The modal data obtained from the finite element model consist of 150 natural frequencies, ω_i; modes, ϕ_i; and modal masses, $m_{mi}, i = 1, \cdots, 150$. Additionally, based on the measurements, the modal damping is assumed to be 1 percent, i.e., $\zeta_i = 0.01$. Based on this information, the state matrix A_s, as in Eq. (43b), is determined by introducing the matrix of natural frequencies, $\Omega = diag(\omega_i)$, and modal damping, $Z = diag(\zeta_i), i = 1, \cdots, 150$.

The determination of matrices B_s and C_s is presented here for the azimuth wheel torque input and the azimuth wheel rate output. For the azimuth wheel torque input, consider the azimuth wheel of radius r_a and the azimuth rail of radius R_a. Let nodes n_1 be located at the contact point of the wheel and the rail. The torque applied to the wheel generates the force F_a at node n_1. The force is tangential to the azimuth rail. Assuming a rigid pinion, the force F_a applied to the wheel is

$$F_a = \frac{T_a}{r_a} \qquad (45)$$

This force has x and y components, F_{ax} and F_{ay} [see Fig. 13(a)], such that

$$F_{ax} = -F_a \cos \alpha_a = -\frac{T_a}{r_a} \cos \alpha_a$$

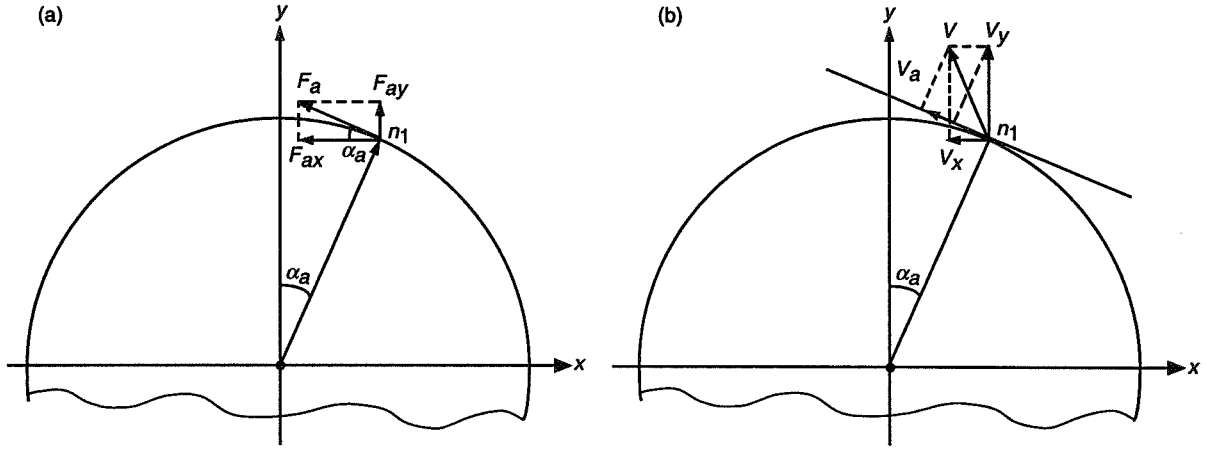$$F_{ay} = F_a \sin \alpha_a = \frac{T_a}{r_a} \sin \alpha_a \qquad (46)$$

Fig. 13. Forces and rates at the azimuth pinion: (a) forces and (b) rates.

and α_a is the angle marked in this figure. Let e_x and e_y denote the unit vector (all but one component are zero, and the nonzero component is equal to one), with the unit component at the location of the x and y displacement of node n_1 in the finite element model. The input, F, to the finite element model is $F = F_{ax}e_x + F_{ay}e_y$. Therefore, B_o follows from the decomposition of F, such that $F = B_o T_a$. From Eq. (46), it follows that

$$B_o = -\frac{e_x}{r_a}\cos\alpha_a + \frac{e_y}{r_a}\sin\alpha_a \qquad (47)$$

Next, from Eq. (43b), it follows that the nonzero (lower) part of B, after introduction of Eq. (47), is

$$M_m^{-1}\Phi^T B_o = -M_m^{-1}\frac{\Phi^T e_x}{r_a}\cos\alpha_a + M_m^{-1}\frac{\Phi^T e_y}{r_a}\sin\alpha_a \qquad (48a)$$

$$= -M_m^{-1}\frac{\phi_x}{r_a}\cos\alpha_a + M_m^{-1}\frac{\phi_y}{r_a}\sin\alpha_a \qquad (48b)$$

where ϕ_x and ϕ_y are vectors of modal components of x and y displacements at node n_1:

$$\left.\begin{array}{l}\phi_x = \Phi^T e_x = [\phi_{x1},\phi_{x2},\cdots,\phi_{x150}]^T \\[2ex] \phi_y = \Phi^T e_y = [\phi_{y1},\phi_{y2},\cdots,\phi_{y150}]^T\end{array}\right\} \qquad (49)$$

where ϕ_{xi} and ϕ_{yi} are x and y displacements of mode i at node n_1. Therefore, from Eqs. (43b) and (48b), one obtains

$$B_s = \left[\begin{array}{c} 0 \\ -M_m^{-1}\dfrac{\phi_x}{r_a}\cos\alpha_a + M_m^{-1}\dfrac{\phi_y}{r_a}\sin\alpha_a \end{array}\right] \qquad (50)$$

The output matrix derivation is presented here for the wheel rate, $\dot\theta_{pa}$. The wheel rotation is

$$\dot{\theta}_{pa} = \frac{v_a}{r_a} \tag{51}$$

where v_a is the tangential velocity of the wheel at the contact point [see Fig. 13(b)]. If v_x and v_y are x and y components of v_a, and α_a is the angle marked in this figure, then

$$v_a = -v_x \cos \alpha_a + v_y \sin \alpha_a \tag{52}$$

therefore,

$$\dot{\theta}_{pa} = \left(-\frac{e_x^T}{r_a} \cos \alpha_a + \frac{e_y^T}{r_a} \sin \alpha_a \right) \dot{q} \tag{53a}$$

and in modal coordinates

$$\dot{\theta}_{pa} = \left(-\frac{\Phi e_x^T}{r_a} \cos \alpha_a + \frac{\Phi e_y^T}{r_a} \sin \alpha_a \right) \dot{q}_m = \left(-\frac{\phi_x^T}{r_a} \cos \alpha_a + \frac{\phi_y^T}{r_a} \sin \alpha_a \right) \dot{q}_m \tag{53b}$$

Finally, the matrix C_s, according to Eqs. (43b) and (53b), is

$$C_s = \left[0 \quad -\frac{\phi_x^T}{r_a} \cos \alpha_a + \frac{\phi_y^T}{r_a} \sin \alpha_a \right] \tag{54}$$

The structural model consists of $m = 150$ modes or 300 states. Modes not participating in system dynamics are eliminated. Observability and controllability properties in the balanced representation are used to determine insignificant modes. The balanced representation [9] is a state–space representation with equally controllable and observable states. The Hankel singular value is a measure of the joint controllability and observability of each balanced state variable. The states with small Hankel singular values are deleted as weakly excited and weakly observed, causing minimal modeling error.

For flexible structures with small damping and distinct poles, the modal representation is almost balanced, c.f. [10–12], and each mode is considered for the reduction separately. For a structure with m modes, matrix B_s has $2m$ rows, and C_s has $2m$ columns. Denote b_s as the last m rows of B_s, c_q as the first m columns of C_s, and c_r as the last m columns of C_s. Then b_{si} is the ith row of b_s, c_{qi} is the ith column of c_q, and c_{ri} is the ith column of c_r. Denote $\beta_{si}^2 = b_{si} b_{si}^T$, $\alpha_{qi} = c_{qi}^T c_{qi}$, and $\alpha_{ri} = c_{ri}^T c_{ri}$. The Hankel singular value for the ith mode is given in [11] and [12]:

$$\gamma_i^2 = \frac{w_{bi} \beta_{si} \sqrt{w_{qi}^2 \alpha_{qi}^2 + w_{ri}^2 \omega_i^2 \alpha_{ri}^2}}{4 \zeta_i \omega_i^2} \tag{55}$$

where the weighting factors $w_{bi} > 0, w_{qi} > 0, w_{ri} > 0$, and $i = 1, \cdots, m$.

Care should be taken when determining Hankel singular values. Units should be consistent; otherwise, some inputs or outputs receive more weight in Hankel singular-value determination than necessary. Consider, for example, the azimuth encoder reading in arcseconds and the elevation encoder reading in degrees. For the same angle, the numerical reading of the azimuth encoder is 3600 larger than the elevation encoder reading; hence, the elements for the azimuth output are much larger than those for elevation.

On the other hand, some variables need more attention than others: Pointing error and encoder readings are the most important factors in the antenna performance; hence, their importance has to be emphasized in mode evaluation. For consistency of units and importance of variables, the weighting factors w_{bi}, w_{qi}, and w_{ri} are introduced. Typically, weights are set to 1.

For each mode, the Hankel singular value is determined and used to decide on the number of modes in the reduced structural model. For the rigid body modes, Hankel singular values tend to infinity; hence, rigid body modes are always included in the reduced model. Hankel singular values of the 150 modes of the antenna model are plotted in Fig. 14. The reduced order model consists of 24 modes: 2 rigid-body modes and 22 flexible modes.

The plots of the transfer function in azimuth and elevation (magnitude and phase) from the wheel (pinion) torque T to the axis rate $\dot{\theta}$ are shown in Fig. 15. They show that the azimuth transfer function has low frequency resonances (about 1.2 and 2.2 Hz), which are absent in the elevation transfer function.
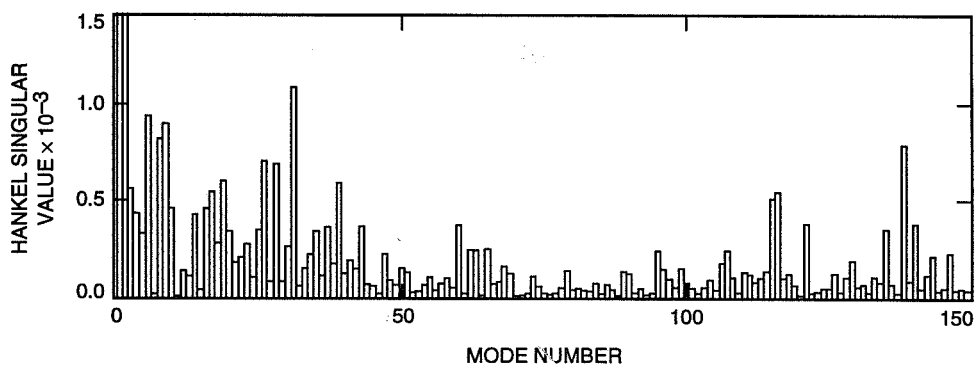

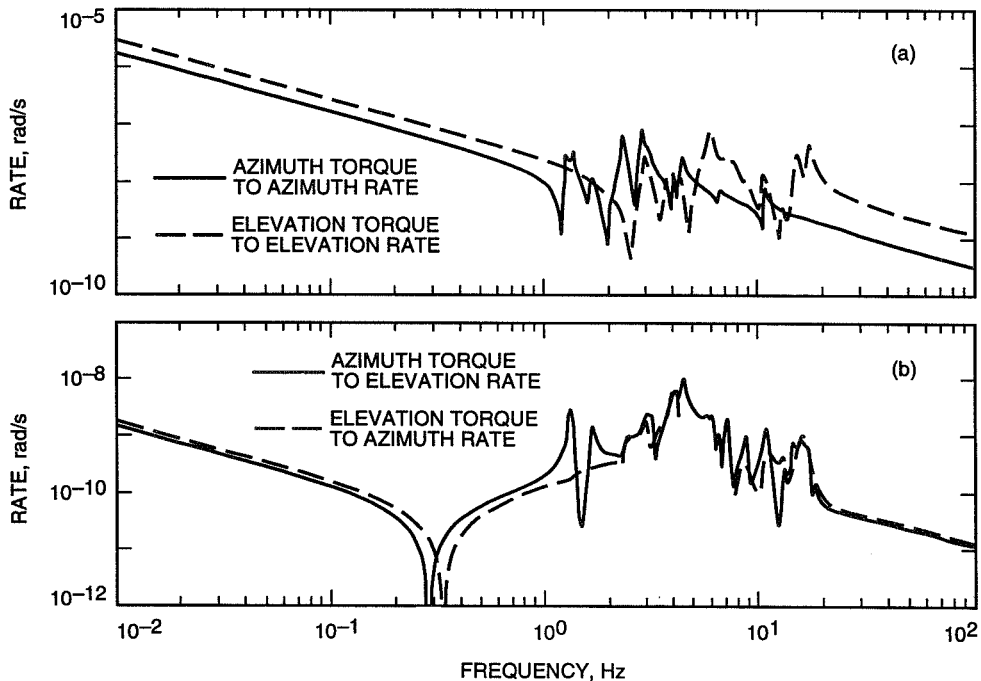Fig. 14. Hankel singular values for the antenna structure.

Fig. 15. Magnitude of the transfer function of the antenna structure: (a) direct coupling and (b) cross-coupling.

IV. Rate Loop Model

A rate loop block diagram is presented in Fig. 16, where T_a and T_e denote the drive torques, $\dot{\theta}_{pa}$ and $\dot{\theta}_{pe}$ denote pinion rates, and r_a and r_e are rate commands in azimuth and elevation, respectively. The state–space equations are combined from the state equations of the azimuth and elevation drives [see Eq. (38) and add subscript "a" for the azimuth drive and subscript "e" for the elevation drive] and the structure [see Eq. (44)]. Combining them, and defining the rate loop state vector x_r as $x_r = [x_{da}, x_{de}, x_s]$, where x_{da} and x_{de} are azimuth and elevation drive states, one obtains the rate-loop state–space equations:

$$\left. \begin{array}{l} \dot{x}_r = A_r x_r + B_{ra} r_a + B_{re} r_e \\[12pt] y = C_r x_r \\[12pt] \theta_a = C_a x_r \\[12pt] \theta_e = C_e x_r \end{array} \right\} \tag{56a}$$

where

$$\left. \begin{array}{l} A_r = \begin{bmatrix} A_{da} & 0 & B_{dta}C_{pa} \\ 0 & A_{de} & B_{dte}C_{pe} \\ B_{sa}C_{da} & B_{se}C_{de} & A_s \end{bmatrix} \\[40pt] B_{ra} = \begin{bmatrix} B_{dra} \\ 0 \\ 0 \end{bmatrix} \\[40pt] B_{re} = \begin{bmatrix} 0 \\ B_{dre} \\ 0 \end{bmatrix} \\[40pt] C_r = \begin{bmatrix} 0 & 0 & C_s \end{bmatrix} \end{array} \right\} \tag{56b}$$

where θ_a and θ_e are azimuth and elevation encoder readings, C_{pa} and C_{pe} are the output matrices for the azimuth and elevation pinion rates, and C_a and C_e are the output matrices for the azimuth and elevation encoders, respectively.

Figure 17 shows the magnitude of the transfer function from the azimuth rate input r_a to the azimuth encoder rate $\dot{\theta}_a$ (solid line) and the magnitude of the transfer function from the elevation rate input r_e to the elevation encoder rate $\dot{\theta}_e$ (dashed line). The figure shows that the required identity relationship for low frequencies is not acquired. The magnitude of the transfer functions for frequencies less than 0.3 Hz is 0.74, below the required 1, due to inaccuracy in the model parameters (mainly in the hydraulic part). This drawback can be removed by the experimental investigation of the parameters of the hydraulic drives, such as motors, valves, and lines. However, this inaccuracy is corrected by the position feedback loop, as will be shown later. The high-frequency peaks in azimuth and elevation (8 Hz in azimuth and 20 Hz in elevation) are the gearbox resonances.
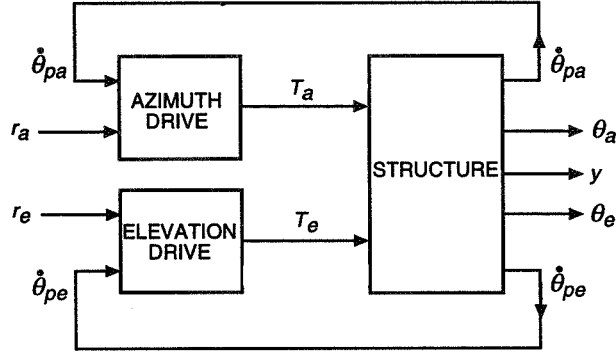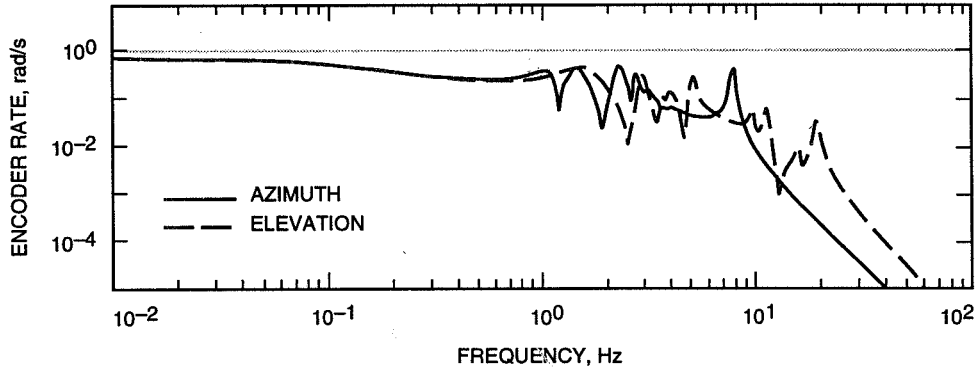
Fig. 16. Block diagram of the rate loop model.

Fig. 17. Magnitude of the transfer function of the rate loop model.

V. Position Loop Model

The rate loop system with the proportional and integral (PI) controller is shown in Fig. 18, where e_a and e_e are the azimuth and elevation servo errors. For the series connection of the rate loop system and the controller, as in Fig. 18(a), define the state vector $x_o^T = [\, x_{ai} \quad x_{ei} \quad x_{rl}^T \,]$ with the new state variables x_{ei} and x_{ai} (integrals of the errors) such that

$$\left. \begin{aligned} \dot{x}_{ai} &= e_a \\[6pt] \dot{x}_{ei} &= e_e \end{aligned} \right\} \tag{57}$$

The system output y is defined in Eq. (56a), the encoder output is $\theta^T = [\, \theta_a \quad \theta_e \,]$, and the input is $e^T = [\, e_a \quad e_e \,]$. The inputs to the rate loop systems are obtained from Fig. 18(a):

$$\left. \begin{aligned} r_a &= k_{pa} e_a + k_{ia} x_{ai} \\[6pt] r_e &= k_{pe} e_e + k_{ie} x_{ei} \end{aligned} \right\} \tag{58}$$

where k_{pe}, k_{ie}, k_{pa}, and k_{ia} are proportional and integral parameters of the controllers. Combining the equations for the rate loop system with Eqs. (57) and (58), one obtains
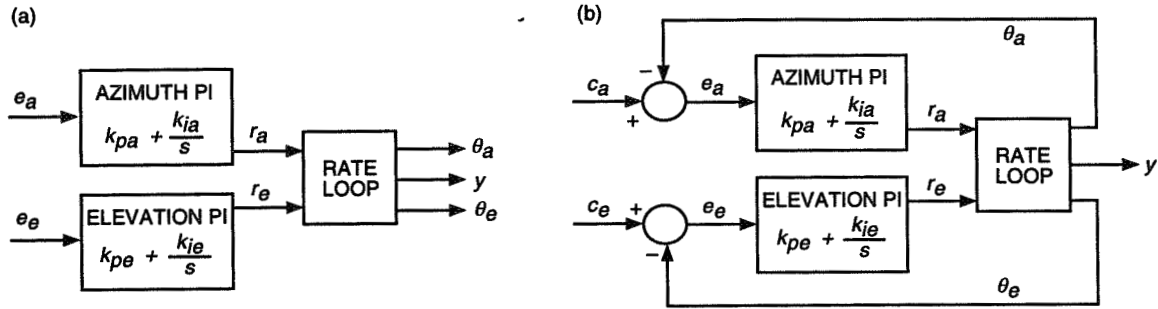
Fig. 18. Position loop: (a) open and (b) closed.

$$\left. \begin{aligned} \dot{x}_o &= A_o x_o + B_o e \\ \theta &= C_o x_o \\ y &= C x_o \end{aligned} \right\} \tag{59a}$$

where

$$\left. \begin{aligned} A_o &= \begin{bmatrix} 0 & 0 & 0 \\ 0 & 0 & 0 \\ k_{ia} B_{ra} & k_{ie} B_{re} & A_r \end{bmatrix} \\ B_o &= \begin{bmatrix} I & 0 \\ 0 & I \\ k_{pa} B_{ra} & k_{pe} B_{re} \end{bmatrix} \\ C_o &= \begin{bmatrix} 0 & 0 & C_a \\ 0 & 0 & C_e \end{bmatrix} \\ C &= \begin{bmatrix} 0 & 0 & C_r \end{bmatrix} \end{aligned} \right\} \tag{59b}$$

For the closed-loop system [see Fig. 18(b)],

$$e = c - \theta \tag{60}$$

where $c^T = [c_a \quad c_e]$ is a command signal in azimuth, c_a, and in elevation, c_e. Introducing Eq. (60) to Eq. (59), one obtains

$$\left. \begin{aligned} \dot{x}_{cl} &= A_{cl} x_{cl} + B_o c \\ y &= C x_{cl} \end{aligned} \right\} \tag{61a}$$

where

$$\mathring{A}_{cl} = A_o - B_o C_o \tag{61b}$$

The simulations shown in Figs. 19 through 22 have two sets of assumptions: (1) a proportional gain of 1 in azimuth and elevation and an integral gain of 0.3 and (2) a proportional gain of 0.7 in azimuth and elevation and an integral gain of 0.2. The closed-loop transfer functions from azimuth command to azimuth encoder are shown in Fig. 19(a), and those from elevation command to elevation encoder are shown in Fig. 19(b). They show a bandwidth of 0.1 Hz. The cross-coupling transfer functions from azimuth command to elevation encoder and from elevation command to azimuth encoder are shown in Fig. 20. They show low-level cross-coupling. The closed-loop step responses from azimuth command to azimuth encoder are shown in Fig. 21(a), and those from elevation command to elevation encoder are shown in Fig. 21(b). They show a 20- to 30-percent overshoot and a 7- to 9-s settling time. The cross-coupling from azimuth step command to elevation encoder and from elevation step command to azimuth encoder is shown in Fig. 22. The cross-coupling is of the order 10^{-3}.
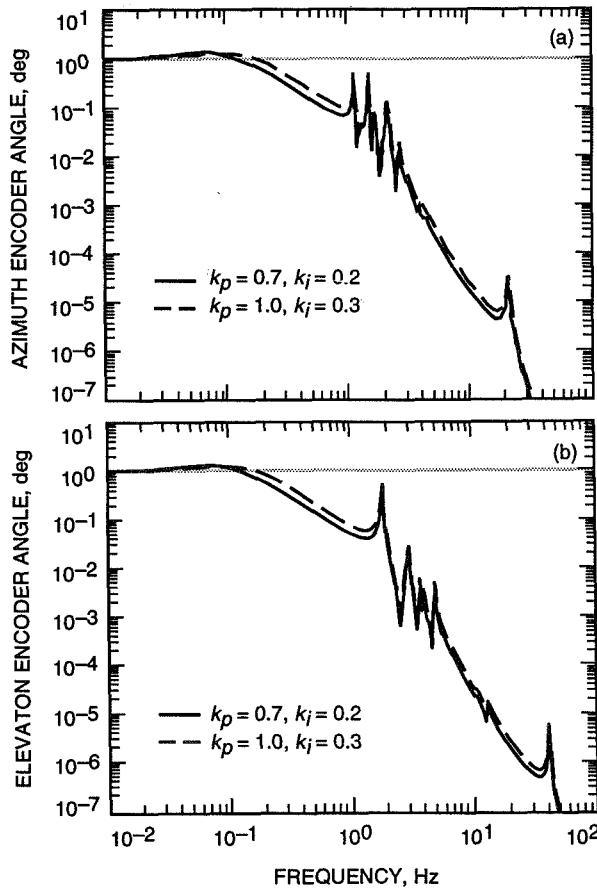

Fig. 19. Magnitude of the transfer function of the closed-loop system: (a) azimuth command to azimuth encoder and (b) elevation command to elevation encoder.
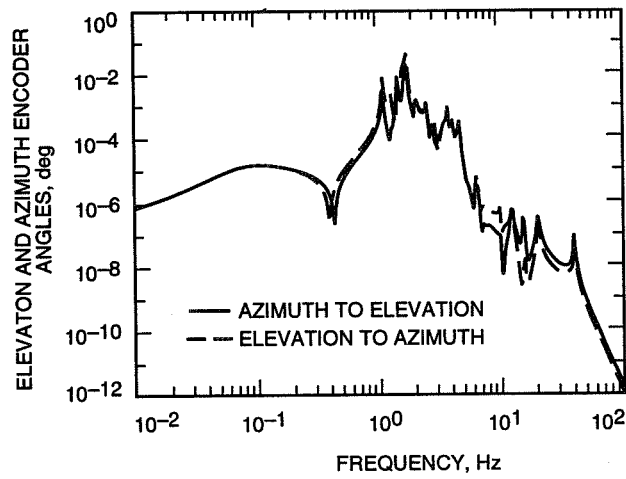
Fig. 20. Magnitude of the transfer function of the closed-loop system: azimuth command to elevation encoder and elevation command to azimuth encoder.
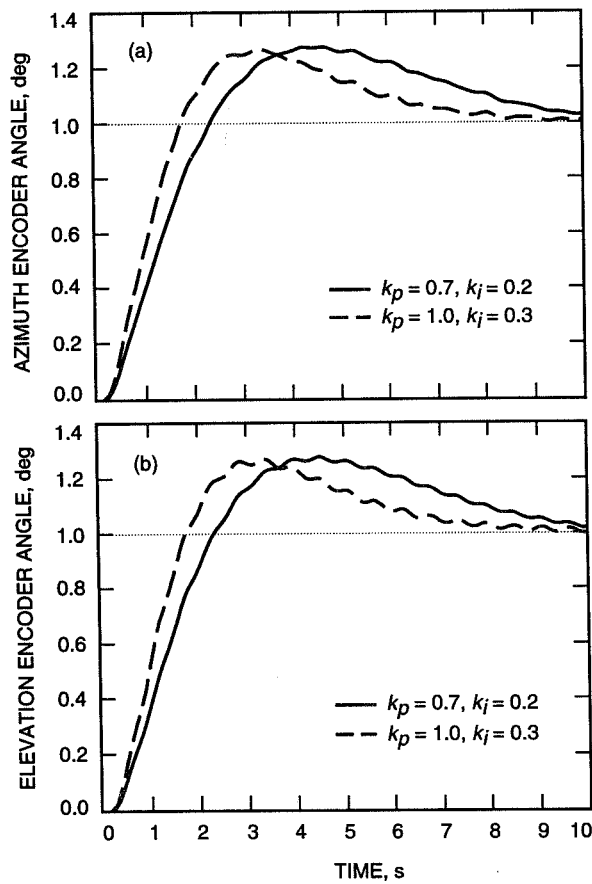

Fig. 21. Step responses of the closed-loop system: (a) azimuth command to azimuth encoder and (b) elevation command to elevation encoder.
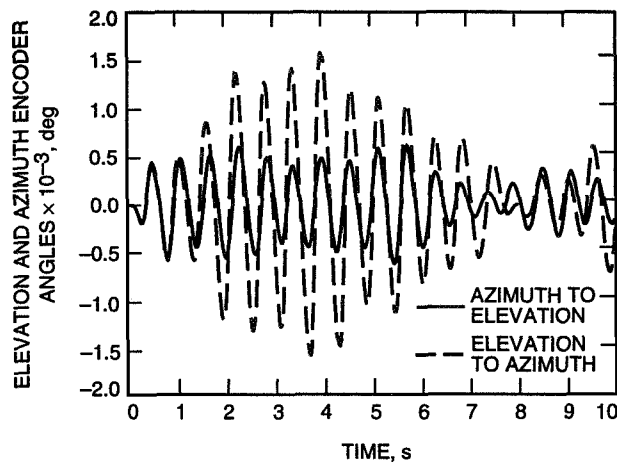
Fig. 22.   Step responses of the closed-loop system: azimuth command to elevation encoder and elevation command to azimuth encoder.

VI. Wind Disturbance Simulations

Wind gust disturbances were modeled similarly to the DSS-13 antenna (see [13]) using the wind tunnel pressure distribution on the dish taken from Blaylock.[1] Their time history is generated using the wind Davenport spectrum (see [14] and [15]), determined for the Goldstone site. The simulations for the 50 km/h wind gave the results listed in Table 4 and compared with the simulation results of the DSS-13 antenna. The table shows that DSS 14 has better disturbance rejection properties (at the encoders) than has the DSS-13 antenna.

Table 4. Servo errors in mdeg (3σ rms) for 50 km/h wind gusts.

Drive	Front wind	Side wind
Elevation, DSS 14	2.6	0.7
Elevation, DSS 13	14.6	1.9
Azimuth, DSS 14	0.1	2.1
Azimuth, DSS 13	0.5	2.3

VII. Conclusions

An analytical model of the DSS-14 antenna has been developed. The rate loop model consists of the structural model (derived from the finite element model), gearbox model, hydraulic servo, and electronic boxes. The position loop was closed, and the time and frequency responses were simulated. The wind pointing errors of the DSS-14 antenna have been simulated. The model allows for detailed simulation of antenna dynamics and for modifications and improvements to the antenna control system.

The simulations confirmed that the use of encoders located at drives limits the performance of the antenna (mainly by reducing its bandwidth to 0.1 Hz). The use of the master equatorial or new encoders

---

[1] R. B. Blaylock, "Aerodynamic Coefficients for Model of a Paraboloidal Reflector Directional Antenna Proposed for a JPL Advanced Antenna System," JPL Interoffice Memorandum CP-6 (internal document), Jet Propulsion Laboratory, Pasadena, California, 1964.

located close to the axes of rotation of the antenna (similarly to the 34-m antennas) would allow expansion of the bandwidth to 0.7–1.0 Hz.

The antenna model needs further improvement. First, in this model, certain parameters of the hydraulic drive are known with rather poor accuracy, and it influences the accuracy of the antenna model. It is essential to use experimental techniques to get more precise values of the parameters. Secondly, the RF pointing errors (in elevation and cross-elevation) of the antenna should be determined in order to evaluate the precision of the antenna pointing.

Acknowledgments

References

[1] R. E. Hill, "A New State Space Model for the NASA/JPL 70-Meter Antenna Servo Controls," *The Telecommunications and Data Acquisition Progress Report 42-91, July–September 1987*, Jet Propulsion Laboratory, Pasadena, California, pp. 247–294, November 15, 1987.

[2] R. E. Hill, "Dynamic Models for Simulation of the 70-m Antenna Axis Servos," *The Telecommunications and Data Acquisition Progress Report 42-95, July–September 1988*, Jet Propulsion Laboratory, Pasadena, California, pp. 32–50, November 15, 1988.

[3] W. Gawronski and J. A. Mellstrom, "Modeling and Simulations of the DSS-13 Antenna Control System," *The Telecommunications and Data Acquisition Progress Report 42-106, April–June 1991*, Jet Propulsion Laboratory, Pasadena, California, pp. 205–248, August 15, 1991.

[4] W. Gawronski and J. A. Mellstrom, "Control and Dynamics of the Deep Space Network Antennas," *Control and Dynamic Systems*, vol. 63, edited by C. T. Leondes, San Diego, California: Academic Press, 1994.

[5] W. Gawronski and J. A. Mellstrom, "Elevation Control System Model of the DSS-13 Antenna," *The Telecommunications and Data Acquisition Progress Report 42-105, January–March 1991*, Jet Propulsion Laboratory, Pasadena, California, pp. 83–108, May 15, 1991.

[6] R. D. Bartos, "Dynamic Modeling of the Servo Valves Incorporated in the Servo Hydraulic System of the 70-Meter DSN Antennas," *The Telecommunications and Data Acquisition Progress Report 42-108, October–December 1991*, Jet Propulsion Laboratory, Pasadena, California, pp. 222–234, February 15, 1992.

[7] R. D. Bartos, "Dynamic Modeling of the Fluid Transmission Lines of the DSN 70-Meter Antennas by Using a Lumped Parameter Model," *The Telecommunications and Data Acquisition Progress Report 42-109, January–March 1992*, Jet Propulsion Laboratory, Pasadena, California, pp. 162–169, May 15, 1992.

[8] R. D. Bartos, "Mathematical Modeling of Bent-Axis Hydraulic Piston Motors," *The Telecommunications and Data Acquisition Progress Report 42-111, July–September 1992*, Jet Propulsion Laboratory, Pasadena, California, pp. 224–235, November 15, 1992.

[9] B. C. Moore, "Principal Component Analysis in Linear Systems, Controllability, Observability and Model Reduction," *IEEE Trans. Autom. Control*, vol. 26, pp. 17–32, 1981.

[10] A. Jonckheere, "Principal Component Analysis of Flexible Systems—Open Loop Case," *IEEE Trans. Autom. Control*, vol. 27, pp. 1095–1097, 1984.

[11] W. Gawronski and J. N. Juang, "Model Reduction for Flexible Structures," *Control and Dynamic Systems*, vol. 36, edited by C. T. Leondes, San Diego, California: Academic Press, pp. 143–222, 1990.

[12] W. Gawronski, *Balanced Control of Flexible Structures*, London: Springer, 1996.

[13] W. Gawronski, B Bienkiewicz, and R. E. Hill, "Wind-Induced Dynamics of a Deep Space Network Antenna," *Journal of Sound and Vibration*, vol. 174, no. 5, 1994.

[14] A. G. Davenport, "The Spectrum of Horizontal Gustiness Near the Ground in High Winds," *Journal of Royal Meteorol. Society*, vol. 87, pp. 194–211, 1961.

[15] E. Simiu and R. H. Scanlan, *Wind Effects on Structures*, New York: Wiley, 1978.

Appendix

Transfer Function Derivation

Each component of the electronics board is composed of operational amplifiers (opamps), resistors, and capacitors. The basic configuration of an inverting opamp circuit is shown in Fig. A-1. The "+" terminal of the opamp is grounded; thus, the "−" terminal voltage is zero, called a virtual ground. In this situation, the currents i_1 and i_2 flowing through impedances Z_1 and Z_2 are equal to

$$\left. \begin{aligned} i_1 &= \frac{v_{in}}{Z_1} \\[2mm] i_2 &= \frac{v_{out}}{Z_2} \end{aligned} \right\}$$

(A-1)

and their sum is zero; that is, $i_1 = -i_2$. Introducing them to Eq. (A-1) gives

$$v_{out} = -kv_{in}$$

(A-2a)

where

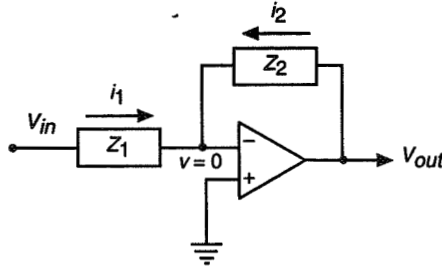$$k = \frac{Z_2}{Z_1}$$

(A-2b)

Fig. A-1. Opamp circuit.

I. Transfer Function G_{to}

A schematic for the transfer function G_{to} is shown in Fig. A-2(a), where the notation and the value of each element were taken from JPL Drawing 9479871D.[2] This schematic can be simplified to the one shown in Fig. A-2(b). In this figure,

$$R_s = \left(R_{56}^{-1} + R_{57}^{-1} + R_{58}^{-1} + R_{59}^{-1}\right)^{-1} + R_{62} = 49.5 \text{ k}\Omega \tag{A-3a}$$

where $R_{56} = R_{57} = R_{58} = R_{59} = 100$ kΩ, and $R_{62} = 24.5$ kΩ; thus, $R_s = 49.5$ kΩ. The component Z_1 is

$$Z_1 = R_{63} + \frac{R_{64}}{1 + R_{64}C_{40}s} \cong R_{63} + R_{64} = 91.1 \text{ k}\Omega \tag{A-3b}$$

where $R_{63} = 40$ kΩ, $R_{64} = 51.1$ kΩ, and $C_{40} = 0.15$ μF. The time constant $R_{64}C_{40} = 0.0077$ s is small, thus neglected. Denote $R_{mta} = 9.7$ kΩ and $R_{mte} = 7.8$ kΩ the motor resistances in azimuth and elevation, respectively, and $C_{41} = 0.15$ μF. Then, the component Z_2 for the azimuth drive is as follows:

$$Z_2 = \frac{R_{mta}}{1 + R_{mta}C_{41}s} \cong R_{mta} = 9.7 \text{ k}\Omega \tag{A-4a}$$

and for the elevation drive,

$$Z_2 = \frac{R_{mte}}{1 + R_{mte}C_{41}s} \cong R_{mte} = 7.8 \text{ k}\Omega \tag{A-4b}$$

The time constants $R_{mta}C_{41} = 0.0015$ s and $R_{mte}C_{41} = 0.0012$ s are of the order 10^{-3} s, thus considered small, and neglected.

The transfer function G_{to} for azimuth is

$$G_{to} = \frac{R_p}{R_s + R_p} = \frac{8800}{49,500 + 8800} = 0.151 \tag{A-5a}$$

and for elevation, it is

---

[2] JPL Drawing 9479871D (internal document), Jet Propulsion Laboratory, Pasadena, California.

$$G_{to} = \frac{R_p^{\cdot}}{R_s + R_p} = \frac{7200}{49,500 + 7200} = 0.127 \qquad \text{(A-5b)}$$

where $R_p = \left(Z_1^{-1} + Z_2^{-1}\right)^{-1} = 8.8$ kΩ in azimuth and 7.2 kΩ in elevation, while $R_s = 49.5$ kΩ.
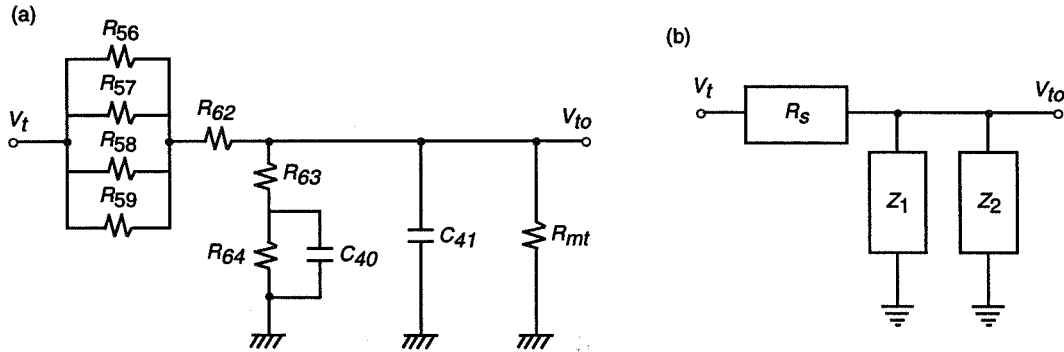

Fig. A-2. Schematic for the transfer function G_{to}: (a) full and (b) simplified.

II. Transfer Functions G_{r1} and G_{r2}

The transfer functions G_{r1} and G_{r2} are determined simultaneously. Their schematic is given in Fig. A-3(a), the parameters parameters of which are

$$\left.\begin{array}{l} R_{15} = 750 \text{ k}\Omega \\[1em] R_{50} = 100 \text{ k}\Omega \\[1em] R_{51} = 12.1 \text{ k}\Omega \\[1em] R_{52} = 442 \text{ k}\Omega \\[1em] R_{53} = 442 \text{ k}\Omega \\[1em] R_{65} = 909 \text{ k}\Omega \\[1em] R_{66} = 90.9 \text{ k}\Omega \\[1em] C_{31} = 1 \ \mu\text{F} \\[1em] C_{42} = 0.1 \ \mu\text{F} \end{array}\right\} \qquad \text{(A-6)}$$

The schematic from Fig. A-3(a) can be transformed to the form shown in Fig. A-3(b). The value of Z_3 is as follows:

$$Z_3 = R_{66} + \frac{R_{65}}{1 + R_{65}C_{42}s} \cong R_{66} + R_{65} = 10^6 \text{ k}\Omega \qquad \text{(A-7)}$$

In this variable, the small time constant $R_{65}C_{42} = 0.0909$ s was ignored.

The value Z_4 is obtained as

$$Z_4 = R_{53} + \frac{R_o}{1 + R_o C_{31}s} = 4.65 \times 10^6 \frac{1 + 0.400s}{1 + 4.205s} \tag{A-8}$$

where $R_o = (R_{50} + R_{52} + R_{50}R_{52})/R_{51} = 4205$ kΩ.

Having determined Z_3 and Z_4, the transfer functions G_{r1} (from v_r to v_s) and G_{r2} (from v_{to} to v_s) are obtained:

$$\left. \begin{aligned} G_{r1} &= \frac{Z_4}{R_{15}} = 6.20 \ G_o \\[2em] G_{r2} &= -\frac{Z_4}{Z_3} = -4.65 \ G_o \end{aligned} \right\} \tag{A-9}$$

where

$$G_o = \frac{1 + 0.400s}{1 + 4.205s} \tag{A-10}$$

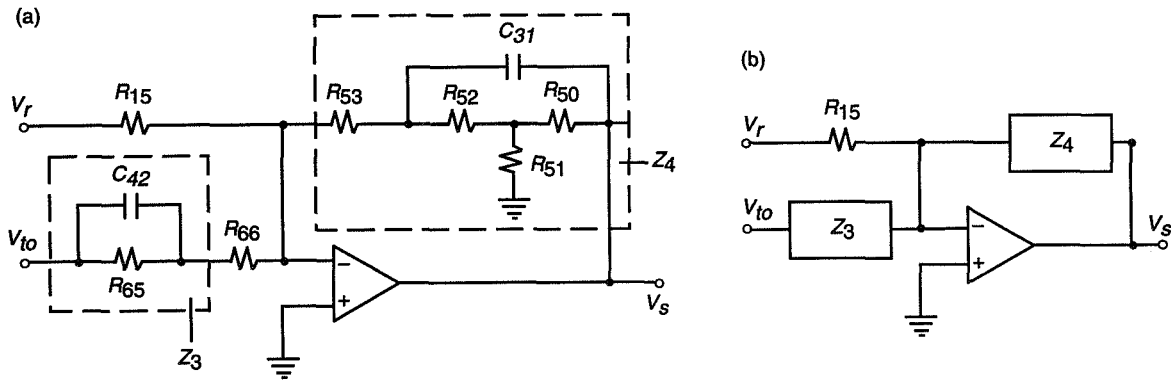is the transfer function of a lag compensator.

Fig. A-3. Schematic for the transfer functions G_{r1} and G_{r2}: (a) full and (b) simplified.

III. Transfer Function G_s

The transfer function G_s is determined from the schematic in Fig. A-4(a), and is shown in compact form in Fig. A-4(b). For this schematic, $R_{13} = 100$ kΩ, $R_{36} = 10$ kΩ, $R_{43} = 24.9$ kΩ, and $C_{18} = 0.1$ μF; therefore, one obtains

$$Z_5 = \frac{R_{36}}{1 + R_{36}C_{18}s} \cong R_{36} = 10 \text{ k}\Omega \tag{A-11}$$

where $R_{36}C_{18} = 0.0015$ s $\cong 0$. Since $v_1 = v_s Z_5/R_{43}$, and $i_s = v_1(Z_5^{-1} + R^{-1})$, thus,

$$G_s = \frac{i_s}{v_s} = \frac{R_{13} + Z_5}{R_{13}R_{43}} = 4.42 \times 10^{-5} \qquad \text{(A-12)}$$
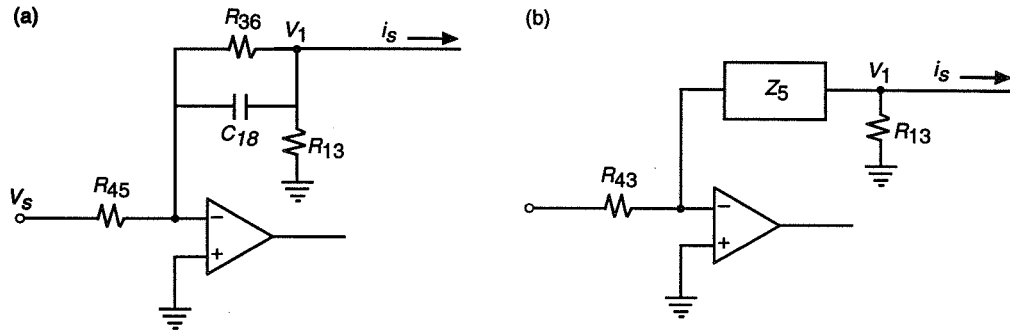

Fig. A-4. Schematic for the transfer function G_s: (a) full and (b) simplified.